This is the accepted version of the paper.

This version of the publication may differ from the final published version.

Computational investigation of porosity effects on fracture behavior of thermal barrier coatings

Jayaprakash Krishnasamy[a,*], Sathiskumar A. Ponnusami[a,b], Sergio Turteltaub[a], Sybrand van der Zwaag[a]

[a]*Faculty of Aerospace Engineering, Delft University of Technology, Kluyverweg 1, 2629 HS Delft, The Netherlands*
[b]*Department of Mechanical Engineering and Aerospace, City University of London, Northampton Square, EC1V 0HB London United Kingdom*

Abstract

The influence of microstructural pore defects on fracture behaviour of Thermal Barrier Coatings (TBC) is analysed using finite element analysis involving cohesive elements. A concurrent multiscale approach is utilised whereby the microstructural features of the TBC are explicitly resolved within a unit cell embedded in a larger domain. Within the unit cell, a random distribution of pores is modelled along with three different layers in a TBC system, namely, the Top Coat (TC), the Bond Coat (BC) and the Thermally Grown Oxide (TGO). The TC/TGO and the TGO/BC interfaces are assumed to be sinusoidal of specified amplitude and frequency extracted from experimental observations reported in the literature. To simulate fracture in the TBC, cohesive elements are inserted throughout the inter-element boundaries in order to enable arbitrary crack initiation and propagation. A bilinear traction-separation relation with specified fracture properties for each layer is used to model the constitutive behaviour of the cohesive elements. Parametric studies are conducted for various pore geometrical features, porosity, fracture properties of Top Coat layer and Thermally Grown Oxide layer thicknesses. The results are quantified in terms of crack initiation and evolution. It is found that the presence of pores has a beneficial effect on the fracture behavior up to a certain value of porosity after which the pores become detrimental to the overall performance. Insights derived from the numerical results can help in understanding the failure behavior of practical TBC systems and further aid in engineering the TBC microstructure for a desired fracture behavior.

Keywords: Thermal barrier coatings, concurrent multiscale model, cohesive elements, porosity, fracture

*Corresponding author

Email addresses: `J.Krishnasamy-1@tudelft.nl` (Jayaprakash Krishnasamy), `sathiskumar.ponnusami@city.ac.uk` (Sathiskumar A. Ponnusami), `S.R.Turteltaub@tudelft.nl` (Sergio Turteltaub), `S.vanderZwaag@tudelft.nl` (Sybrand van der Zwaag)
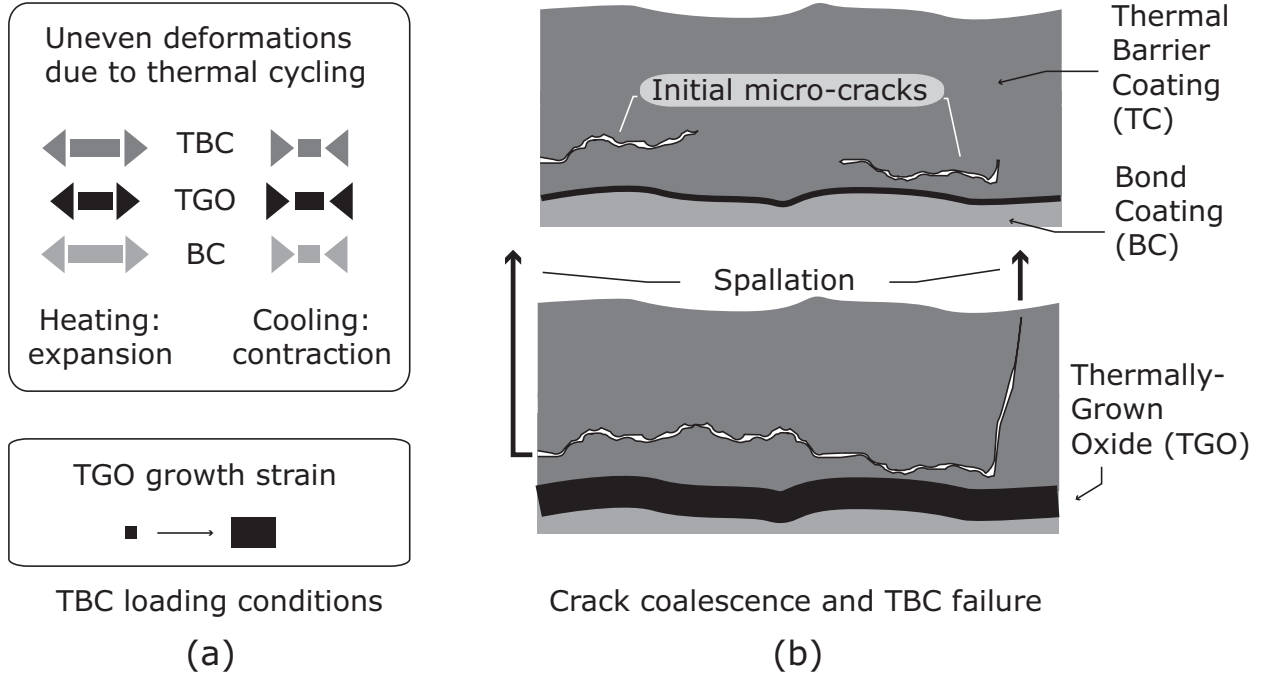
Figure 1: A schematic TBC system showing the failure mechanisms and the governing loading conditions.

1. Introduction

In aerospace and power gas turbine engines, the turbine blades need to operate at very high temperatures for enhanced thermodynamic efficiency of the overall power cycle. During transient or prolonged periods, the temperature can exceed 1100 °C. To withstand such harsh thermal environment, ceramic coatings are applied onto the metallic blades providing the necessary protection against severe thermal degradation. Such protective coatings are termed as Thermal Barrier Coatings (TBC). A typical TBC system consists of three different layers, namely a ceramic Top Coat (TC), an active Thermally Grown Oxide (TGO) layer and a metallic Bond Coat (BC), see Fig. 1. Owing to such layered architecture made of different materials, thermal stresses are generated when the TBC system is subjected to thermal cycles, a typical loading condition experienced for example in a jet turbine engine during flight. Such thermal stresses in combination with stresses associated with the continual growth of the TGO layer initially lead to the formation of microcracks [1, 2] in the TBC and ultimately result in failure of the TBC system. Spallation, which is the mechanical separation of the coating from the substrate, is illustrated in Fig. 1. Failure by spallation implies that the underlying structural components are directly exposed to the high-temperature environment, which degrades the blade and, in turn, may eventually cause catastrophic engine failure.

The failure mechanisms discussed above are primarily influenced by the TBC's microstructural features [3, 4, 5, 6] which are governed by processing and spraying parameters [7, 8, 9, 10, 11]. In air plasma sprayed TBC, the microstructure is characterized by the

2

presence of splats, pores and pre-existing microcracks, in addition to the presence of irregular and rough interface between the layers. Various measurement techniques have been used to quantify the microstructural features, in particular pores and interface morphology of the plasma sprayed TBC [12, 13, 14, 15, 16, 17, 18]. These quantification can be further used to correlate the microstructure of the TBC with its material properties and lifetime. From an experimental viewpoint, there has been a significant interest in understanding the influence of microstructure on the thermo-mechanical properties and the lifetime of TBC [19, 20, 7, 9, 21, 22, 23, 24, 25]. Numerical studies of defects in TBCs such as pores and pre-existing cracks, have been focussed primarily on evaluating their influence on thermal conductivity [26, 27], thermo-elastic properties [28, 29] or stress distribution [30] using analytical and/or numerical methods

Regarding the analysis of failure in TBC systems, earlier research has been focussed on studying the relation between interface irregularities and interface crack nucleation and propagation [31, 32, 33]. A detailed review on finite element studies to model the thermal and the failure properties of TBC systems can be found in [34]. However, most of the existing studies do not explicitly account for the presence of the microstructural defects, in particular pores. The effect of pores on the failure of ceramics have been studied in [35]. Their analysis, however focusses on the bulk material under mechanical loading and does not include a coating system under thermo-mechanical loading. In [36], a numerical sample generated from micrographs of a real air plasma sprayed (APS) TBC, which included pores, was used to simulate its failure. However, the analysis was limited to a single sample under purely mechanical loading and therefore could not establish a systematic relation between porosity and fracture properties during thermal cycling.

It is the objective of the present research to systematically analyze the effect of pores in the TC ceramic layer on the fracture mechanisms of TBC systems in particular for the case of thermal cycling. The effect of porosity is investigated in detail using two sets of simulation. The first set refers to microstructures with controlled characteristics such as porosity, pore size distribution, pore aspect ratio and pore orientation. The goal is to study the influence of each of those features on the failure behavior of TBCs. The second set of simulations is used to study the interaction between the porosity, the fracture properties of the TC layer and the thickness of the TGO. To minimize the influence of a specific microstructural feature, the pore size, pore orientation and pore aspect ratio are randomly distributed in the second set of simulations. The concurrent multiscale finite element setup is used for this study in order to also include free edge effect in the TBC system. Due to computational cost a two dimensional plane strain framework is adopted. Consequently, the findings of the present study are meant to provide qualitative insights of the influence of pores on the damage nucleation and propagation of cracks in TBC systems.

2. Multiscale finite element model of TBC

The modelling setup considered in this work is based on disk-shaped APS TBC samples used to experimentally characterize the microstructure of APS TBC coatings and to determine their lifetime upon thermal cycling [37] see Fig. 2.a. Most of the modelling approaches

3

in the literature [38, 32, 39] utilize a computational cell where the individual layers of the TBC are modelled in detail without considering the substrate. The effect of the substrate is included through enforcing appropriate boundary conditions derived from the substrate deformation under thermal loading. In contrast, a concurrent multiscale approach is adopted in the current work which enables the effect of substrate to be accounted for directly. This modelling involves a two-scale approach in which an explicitly resolved TBC computational cell is embedded in a much larger domain of the TBC, as shown in Fig. 2. The explicitly modelled pores allow to perform a detailed study of their effect on TBC failure mechanisms. For simplicity, a plane strain formulation is used in the simulations. In this approach, the boundary conditions of the embedded computational cell are automatically applied by the surrounding large domain of the TBC. Furthermore, it has been experimentally observed that damage often initiates at the free edge of the sample [40, 41, 42]. In order to include the free edge effect the explicitly resolved TBC computational cell is embedded at the edge of the sample, as shown in Fig. 2.b and Fig. 2.C.
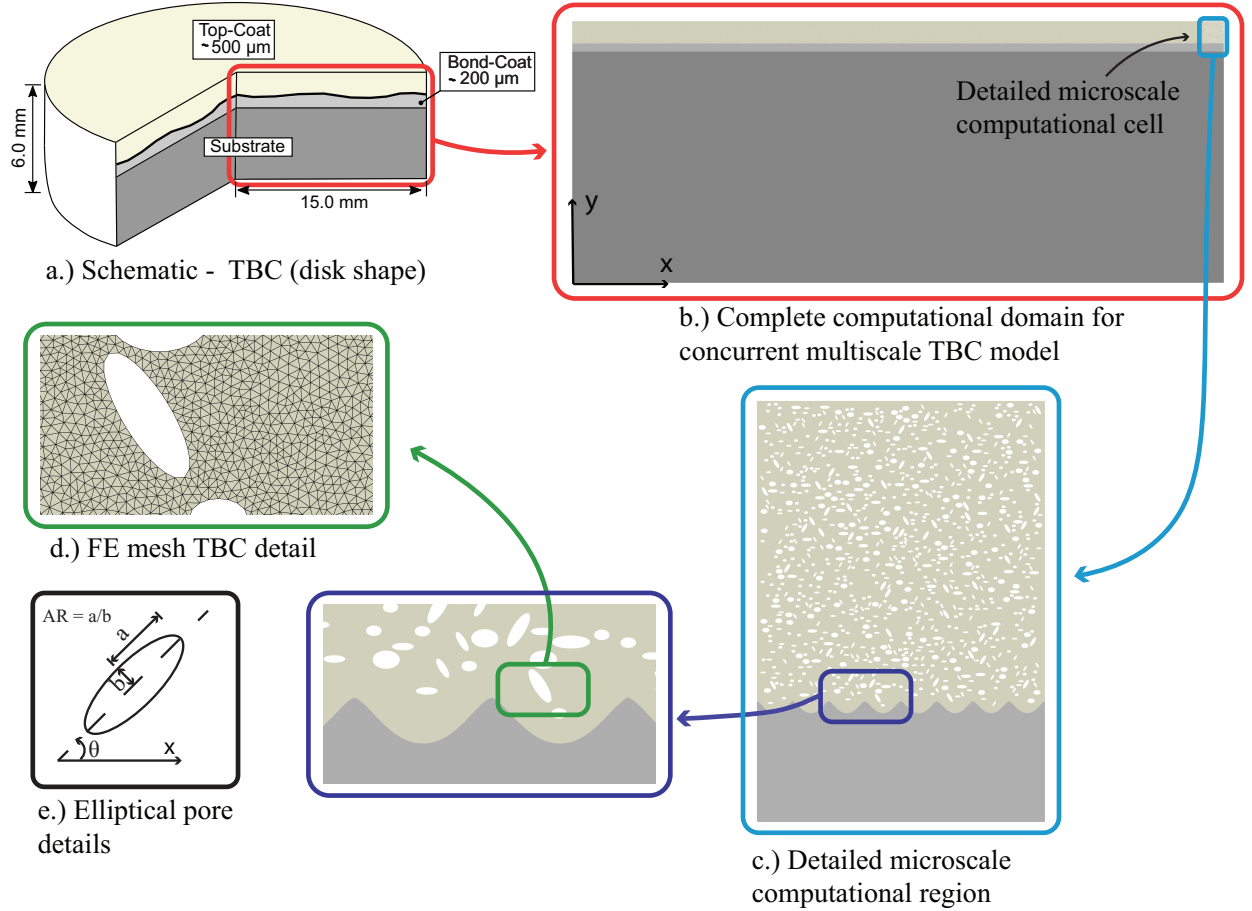

Figure 2: A schematic of disk-shaped TBC system and the corresponding finite element geometry

The thickness of the TC, BC and substrate are given by $h_{TC} = 500$ μm, $h_{BC} = 200$ μm and $h_{sub} = 5.3$ mm respectively. The radius of the disk-shaped sample is given by W =

15 mm. The width of the computational cell is w= 480 μm which is based on the domain convergence analysis carried out in [38]. The thickness of the TGO layer is taken as zero for the first set of simulations and it is varied for the second set of simulations.

In the concurrent multiscale finite element model, the microstructural features related to pores and interface roughness are considered, as highlighted in Fig. 2. An idealized sinusoidal curve is used to model the interface morphology between the TC and the BC. The specified wavelength and amplitude for the sinusoidal interface is 60 μm and 10 μm respectively [38]. In the outer region of the TC layer the pores are included through effective elastic properties to reduce the computational time by using a coarser mesh. The pores are modelled as ellipses randomly distributed in the TC layer of the embedded computational cell for a given volume fraction (i.e., porosity). The fracture behavior of the TBC is incorporated in
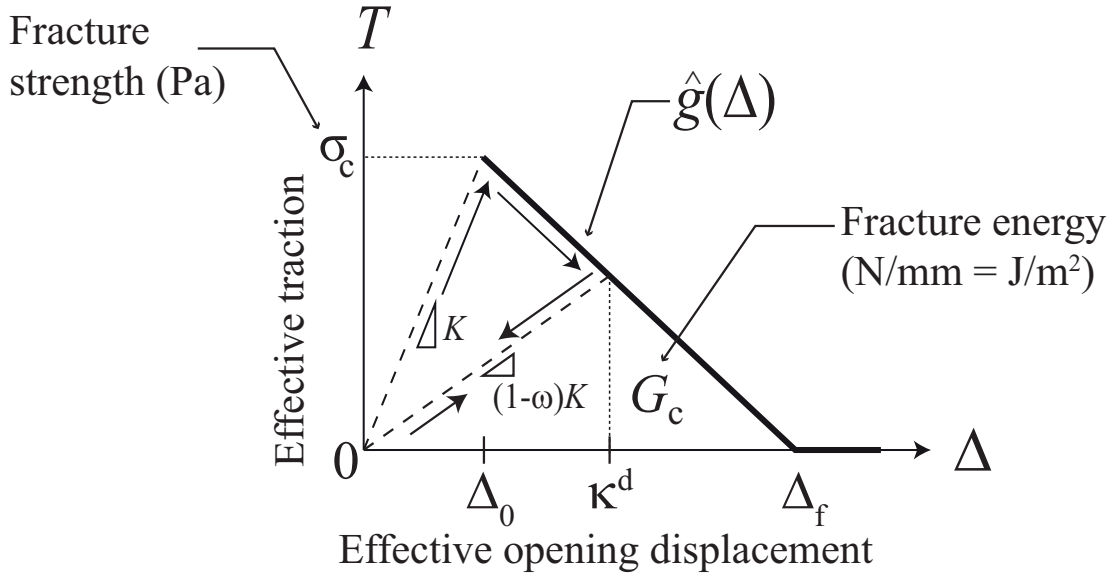

Figure 3: A bilinear traction-separation law to simulate the fracture process in TBC. The arrow shows the loading, damage, unloading and reloading constitutive behavior

the analysis using a cohesive zone model that simulates fracture as a gradual phenomenon of formation of two new surfaces. It replaces the traditional crack tip stress singularity with a process zone (i.e cohesive zone) which is bounded by the cohesive strength of the material. The typical constitutive behavior of the cohesive zone model is governed by the fracture properties of the material. In the finite element framework the cohesive zone model is implemented by using a zero-thickness cohesive element. It is also important to note the fracture process is modelled in the embedded computational cell only and the outer regions of the TBC exhibits only an elastic response. The bi-linear cohesive law [43] used in this work to describe the effective traction-separation behavior of the cohesive surface is shown in Fig. 3. The values for the maximum effective traction and area under the curve in Fig. 3

correspond to the fracture strength and fracture energy of the material, respectively. The initial response of the cohesive surface before damage initiation is governed by the cohesive stiffness (K). The artificial compliance introduced by the cohesive stiffness is alleviated by choosing sufficiently higher values for K. The elastic bulk response of the material is modelled using two-dimensional three-noded plane strain triangular elements. The modelling and the meshing of the finite element model is carried out using the open source software GMSH [44]. The cohesive elements are inserted at all the bulk element interfaces of the computational cell by modifying the initial finite element mesh through a MATLAB script. The process of inserting the cohesive element through out the mesh enables the arbitrary crack initiation and propagation in the computational cell which is a necessary condition to predict the failure behavior of such complex system. A fine mesh size of 1 μm is used in the computational cell region to obtain the converged fracture pattern and to resolve the extent of the cohesive zone properly. As discussed above, the elastic region of the TBC domain is coarsely meshed with a size of 150 μm to reduce the computational costs.

2.1. Loading and boundary conditions

A typical thermal cycle of a TBC consist of three phases namely a heating phase, a dwell phase and the cooling phase. In the heating phase, the temperature of the TBC is increased from room temperature to the operating temperature and, in the dwell phase, the temperature remains constant at the operating value. Finally, in the cooling phase, the temperature is decreased to the room temperature. The TBC is assumed to be stress-free in the dwell phase as such coatings are deposited at a temperature similar to the operating temperature. Hence, the loading condition considered is a thermal contraction (cooling phase) where the cracks are likely to initiate and grow due to thermal mismatch stresses. For the finite element simulation, temperature is gradually decreased from a typical TBC operating temperature of 1100° C to 30° C. In addition, the symmetry of the geometry shown in Fig. 2.a is utilized in the TBC finite element setup. The simulations are conducted in software package Abaqus using an implicit Newton-Raphson iterative solver. The cooling rate doesn't play a role as the simulations are based on quasi-static analysis.

2.2. Constitutive models and material properties

The constitutive material behavior of the different layers of the TBC is assumed to be linear elastic and isotropic. The elastic, thermal and fracture properties used for individual layers are summarized Table 1. The material properties summarized in Table 1 corresponds to an air plasma sprayed Yttria Stabilised Zirconia (YSZ)-based TBC system. While the TC layer is composed of YSZ, the BC layer is made of NiCrAlY alloy. The TGO layer, formed during operation, is composed of alumina (Al_2O_3) and the substrate is a nickel alloy typically used in a aircraft gas turbine blades. The material properties of BC and the substrate are similar to the values used in earlier work [38]. The elastic and fracture properties of the TC and the TGO layer are in accordance with [45]. Different values of normal strength σ_n and shear strength σ_s are used for the TC and TGO layer, defined by the parameter γ, the shear strength to the normal strength ratio. A value of $\gamma = 4$ is assumed to prevent the shear failure of TBC. This assumption is based on experimental observations of TBC failure

6

Layers	E (GPa)	ν	α (10^{-6} 1/°C)	σ_n (MPa)	G_{IC} (N/mm)	γ
TC	200	0.15	12.5	200	0.008	4
BC	130	0.3	14.5	500	0.3	1
TGO	380	0.15	6	380	0.06	4
Substrate	200	0.28	16	-	-	-

Table 1: Elastic and fracture material parameters of the TBC components.

which shows that TBC predominantly fails in mode I. The fracture toughness in mode I and mode II are also varied with same parameter γ in the current study. The pore defects in the outer (elastic) TC layer are accounted through an effective (reduced) elastic modulus of 80 GPa. The interface between TC with BC or TGO layer is assumed to have the same fracture properties as the TGO layer.

3. Results and discussions

As discussed in the Sec. 1, two sets of analyses were conducted and the resulting fracture characteristics are discussed. The first set aims to study the effect of various microstructural features governing the TBC behavior through parametric simulations. The second set considers a TBC computational cell with randomly generated microstructural features which is used to study the interaction between the porosity, the fracture properties of the TC layer and the thickness of the TGO. The results are summarized in terms of crack initiation temperature and crack length at the end of the considered thermal cycle for each parametric case. The crack initiation temperature is defined based on a predefined crack length (sum of the length of all failed cohesive elements) to avoid mesh dependency. Three different lengths of 1, 2 and 3 μm are considered to predict the influence of predefined crack length on crack initiation temperature. The percentage of error for the length of 2 and 3 μm is less than 5 %. Hence, the predefined total crack length of 3 μm is considered as a representative value for all the parametric simulations to define the crack initiation temperature. The cohesive element is said to be failed when it dissipated 95 % of the fracture energy. The TC layer is said to be completely failed if it becomes disconnected from the BC and/or TGO layers in the computational cell.

3.1. TBC with parametrically varied pore features

In this set of analyses, various pore characteristics are varied, including size, aspect ratio, orientation and overall volume fraction (porosity) as listed in Table 2. Like any parametric analysis, while studying the influence of a given pore feature, the other features are kept constant. Five realizations, each with a distinct spatially random pore distribution, are considered for each parametric case and the results are plotted in terms of the average along with the scatter. The results corresponding to the applied single thermal cycle are reported in terms of crack initiation temperature and total crack length.

Pore features	Geometrical Parameters
Porosity(V_f)	0, 10, 15, 20, 30
Aspect ratio(AR)	1.5, 3, 4.5
Orientation(θ)	0, 45, 90, 135 deg
Size	25, 50, 100 μm^2

Table 2: Summary of pore geometric parameters used.

3.1.1. Effect of porosity

In this section, the volume fraction of the pores is varied and its influence on crack initiation temperature and total crack length are reported in Fig. 4. Five different pore volume fractions given by $V_f = 0$, 10, 15, 20 and 30 % are considered. The crack initiation temperature remains almost constant for the range of porosity analyzed. In terms of crack length, the results indicate that there is an initial decrease in damage and subsequently an increase until complete failure for a porosity of 30%. The porosity of 15% appears as an optimal value in terms of crack length (less damaged configuration). Note that the fully dense TC layer shows a higher crack length compared to the porous TBC up to 20%. This is due to the fact that the presence of pores increases the TBC compliance which reduces the strain energy contribution to the crack driving force [46]. Experimental studies in the literature also revealed a positive influence of pores, whereby it was observed that presence of the pores improved the lifetime of the TBC [47].
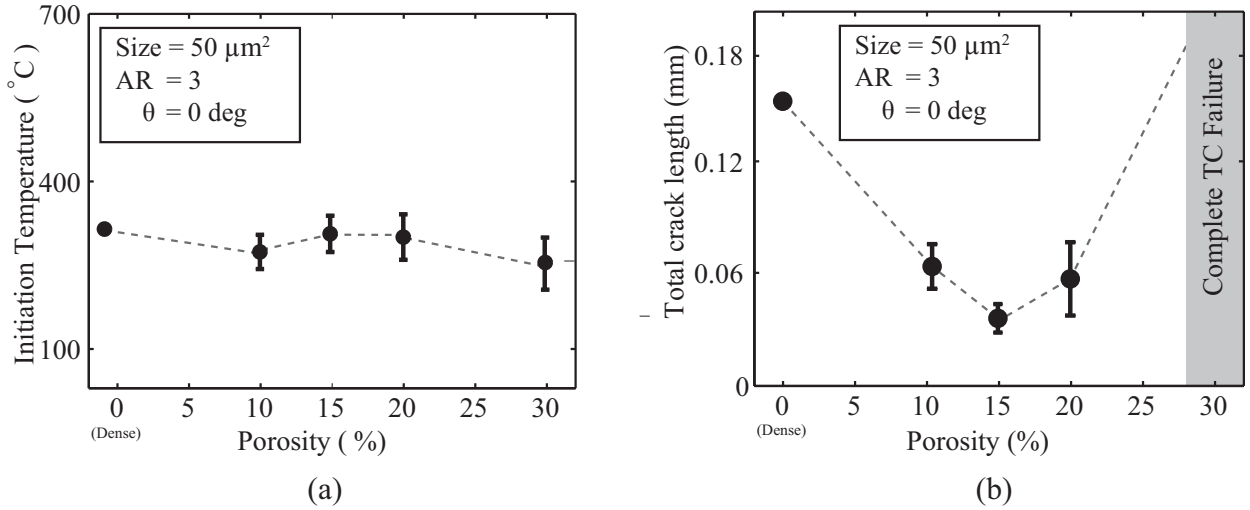

Figure 4: Variation of (a) crack initiation temperature and (b) total crack length for different pore volume fraction 0 (dense), 10, 15, 20 and 30 % with the fixed pore size of 50 μm^2, aspect ratio of 1.5 and orientation of 0 deg

8

3.1.2. Effect of pore size

Three different pore sizes defined by a cross-sectional pore area of 25, 50 and 100 μm^2 are considered in this analysis. The pores are assumed to be elliptical with an aspect ratio of 1.5 and an orientation angle of 0 deg. The pore volume fraction is also fixed and equal to 15%. The simulation results are presented in terms of crack initiation temperature and total crack length as shown in Fig. 5. For comparison purposes, the results of a fully dense TBC (defined as a zero pore size) are also plotted in Fig. 5. From Fig. 5.a, it can be observed that the crack initiation temperature increases gradually with increasing pore size, thus resulting in earlier crack initiation. When compared with a fully dense TBC (no pores),the TBC with 15 percent pore volume fraction and a pore size of 100 μm leads to an early crack onset, i.e., the crack initiation temperature is increased from 300° C to 400° C. Such a trend in the crack initiation behavior can be attributed to the amplified stress concentration effects as the pore size is increased. In terms of the crack length, increasing the pore size leads to a larger crack length at the end of the cooling cycle as shown in Fig. 5.b. It is worth noting that the crack initiation temperature increases linearly with respect to the pore size. Similar observations are also reported in [48, 49] based on experiment study on ceramics with different pore sizes. Similarly, the crack length increases approximately linearly with increasing pore size, as seen in Fig. 5.b. Thus, in general, it can be concluded that an increase in the pore size is generally detrimental to the TBC integrity. Nonetheless, the crack length with pores remains smaller than the fully-dense case. Hence, a 15% porosity with small pores appears to be optimal.
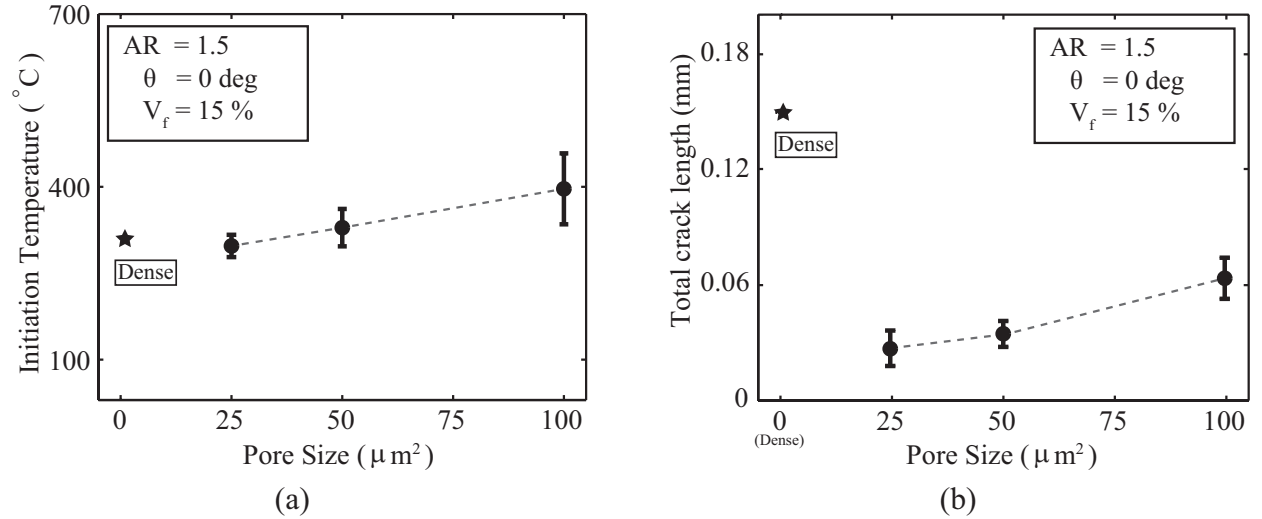

Figure 5: Variation of (a) crack initiation temperature and (b) total crack length for different pore size 0 (dense), 25, 50 and 100 μm^2 with the fixed pore aspect ratio of 1.5, orientation of 0 deg and volume fraction of 15%.

3.1.3. Effect of pore aspect ratio

To investigate the effect of pore aspect ratio, three different aspect ratios are analyzed, namely 1.5, 3 and 4.5. The values for pore size, orientation and volume fractions are fixed

and are given by 50 μm^2, 0 deg and 15 %, respectively. The results of the simulations are summarized in Fig. 6 along with the results of fully dense TBC (referred to as zero aspect ratio). A similar trend as with the effect of pore size is observed whereby the crack initiation temperature and the crack length increase with increasing pore aspect ratio. Although no experimental results for this specific parameter seem to be available in the literature, it is worth noting that, a similar type of behavior is reported for SiC ceramic materials in [50] using discrete element simulations under uni-axial compression. This observation is due to the fact that as the pore aspect ratio is increased, the stress concentration around the pores is increased leading to earlier crack initiation and increased total crack length. In other words, as the aspect ratio is increased, the pores tend to act more like a crack, resulting in easier crack initiation and propagation. Further, the stress concentrations arise due to the interaction of multiple pores in their vicinity, leading to the overall reduced integrity of the TBC.
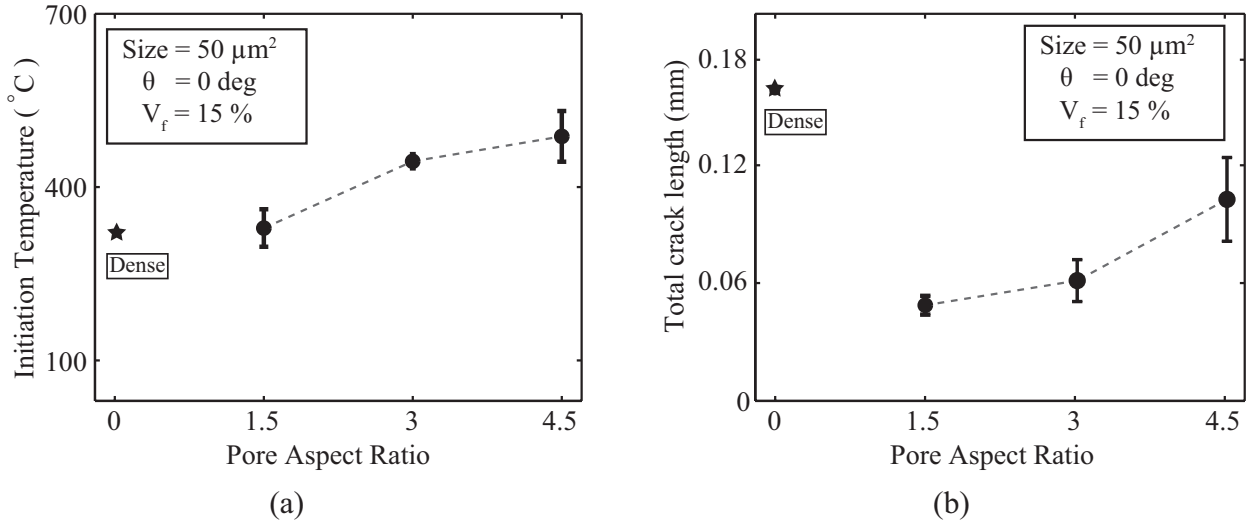

Figure 6: Variation of (a) crack initiation temperature and (b) total crack length for different pore aspect ratio 0 (dense), 1.5, 3 and 4.5 with the fixed pore size of 50 μm^2, orientation of 0 deg and volume fraction of 15%.

3.1.4. Effect of pore orientation

Another parameter of interest is the pore orientation for elliptical pores. To study the effect of pore orientation, three different values are considered given by 0, 45, 90 and 135 degrees with 0 deg corresponding to an elliptical pore with the semi-axis oriented parallel to the TGO (see Fig. 2.e). The volume fraction and the aspect ratio of the pores are kept constant at 15% and 1.5 respectively.

The results obtained from the analysis from five different realizations for each case are summarized in Fig. 7. Unlike in the case of pore size variations, the crack initiation temperature and in particular in crack length does not vary monotonically with the orientation angle. Increasing the pore orientation from 0 deg (horizontally oriented pores) delays the
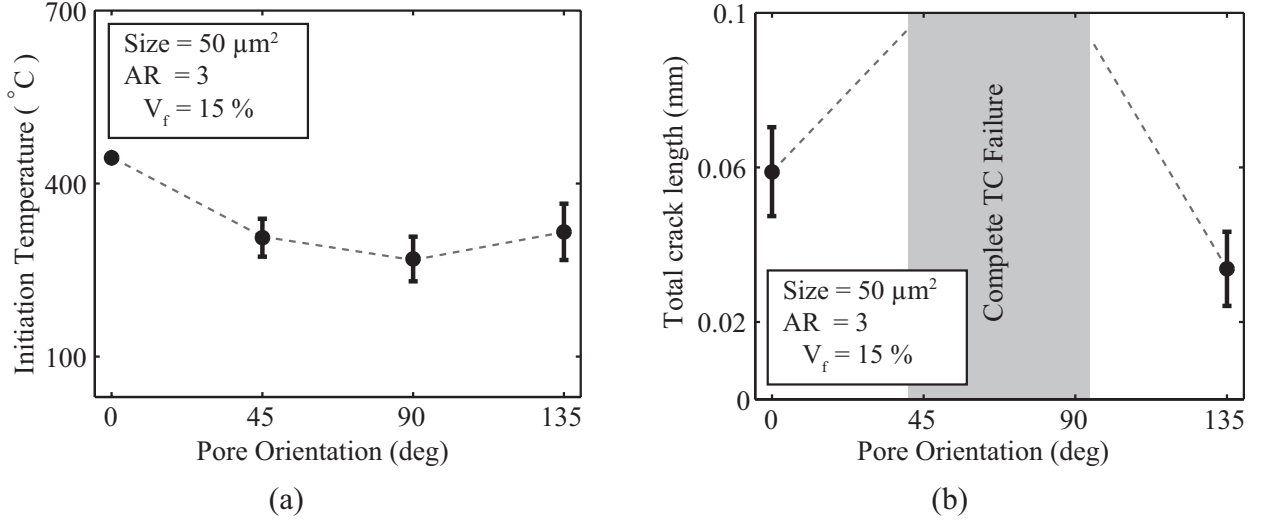
10

Figure 7: Variation of (a) crack initiation temperature and (b) total crack length for different pore orientation 0, 45, 90 and 135 deg with the fixed pore size of 50 μm^2, aspect ratio of 3 and volume fraction of 15%.

crack initiation as can be observed from Fig. 7.a. This is expected as the horizontally oriented pores offers a more favorable configuration for the micro cracks to originate and coalesce as compared to the more vertically aligned pores. The initiation temperature is symmetric with respect to 90 deg as expected. However, the total crack length is not symmetric, which is due to the influence of the free edge, either promoting crack extension or reducing it.

3.2. TBC with random microstructural pores

In this section, a TBC computational cell is considered with random pore features that are similar to actual TBC microstructures [37]. The values of the pore features used in the modelling for four different porosities are given in Table 3. Similar to the parametric case, the pores are approximated as ellipsoidal entities with their aspect ratio (AR), orientation (θ) and size (pore area). The number of small pores (SP) and large pores (LP) are obtained from the corresponding size and the porosity. The assignment of orientations and aspect ratios are also indicated in the Table 3. Once each pore has been assigned a size, aspect ratio and orientation, its spatial location within the TBC computational cell is determined using a uniformly distributed random number for each spatial coordinate of its centre. Pores are regenerated to prevent overlaps. Five different realizations are considered for the same set of pore features given in Table 3 in order to study the effect of such spatially random distribution on the TBC fracture characteristics.

For each realization, the TBC system is subjected to the thermal contraction load as the temperature is decreased from 1100°C to 30°C . Stress distribution plots along with the crack evolutions at the end of the thermal loading step for one of the realizations are shown in Fig. 8. The insets in the figure correspond to the stress contours for the concurrent multiscale model. In particular, the figure illustrates the cracking that occurs at the TC/BC interface due to their mismatch in CTE as well as the free edge effect whereby cracking initiates at the free surface (see Fig. 8.c and Fig. 8.d). The presence of microstructural pores in the TC

11

Geometrical features	Modelling parameters (%)			
Porosity (V_f)	10	15	20	30
Micro-porosity [SP] (Size = 25 μm^2)	5	7.5	5	15
Macro-porosity [LP] (Size = 75 μm^2)	5	7.5	15	15
Round shaped porosity (AR = 1.5) [LP , SP]	5 [2.5 , 2.5]	8 [4 , 4]	11 [8.5 , 2.5]	16 [8 , 8]
Lamellar shaped porosity (AR = 3)	5	7	9	4
Horizontal lamellar porosity (θ =0 deg) [LP , SP]	2.5 [1.25 , 1.25]	3.5 [1.75 , 1.75]	5 [1.5 , 3.5]	7 [3.5 , 3.5]
Inclined lamellar porosity ($\theta = \pm45$ deg) [LP , SP]	2.5 [1.25 , 1.25]	3.5 [1.75 , 1.75]	4 [1 , 3]	7 [3.5 , 3.5]

Table 3: Modelling parameters generated for random features

layer leads to a complex variation in stress fields [4, 30] as expected. As shown in Fig. 8.a and Fig. 8.b, the BC region close to the free edge and near the TC/BC interface is under a tensile stress in x direction (σ_{xx}). On the other hand, the tensile stress in the vertical direction (σ_{yy}) arising out of the free edge and the stress concentration due to pores induces the mode I edge cracking of the TC layer [51] away from the TC/BC interface as observed in Fig. 8.d. The shear stress distribution (σ_{xy}) for the embedded computational cell is shown in Fig. 8.b which may appear to be critical especially in the lower part of the TC layer. However, as discussed in Sec. 2.2, higher fracture values are used for mode II, in order to prevent the shear failure of the TBC. The interior regions of the TC layer experience the formation of microcracks close to the TC/BC interface under mixed mode conditions and are shown in Fig. 8.c. The variation of crack initiation temperature and the total crack length with the porosity is presented in Fig. 9. Comparing the results shown in Fig. 9.a and Fig. 9.b with the corresponding data in Fig. 4.a and Fig. 4.b (porosity), it can be concluded that the random microstructure predicts similar values as the controlled microstructure but the scatter in the latter is higher. This may be ascribed to the fact that the random microstructure contains a mix of factors that may increase but also decrease the initiation temperature and the total crack length (i.e., the random microstructure contains pores with large but also small aspect ratios, pore sizes and various orientations).
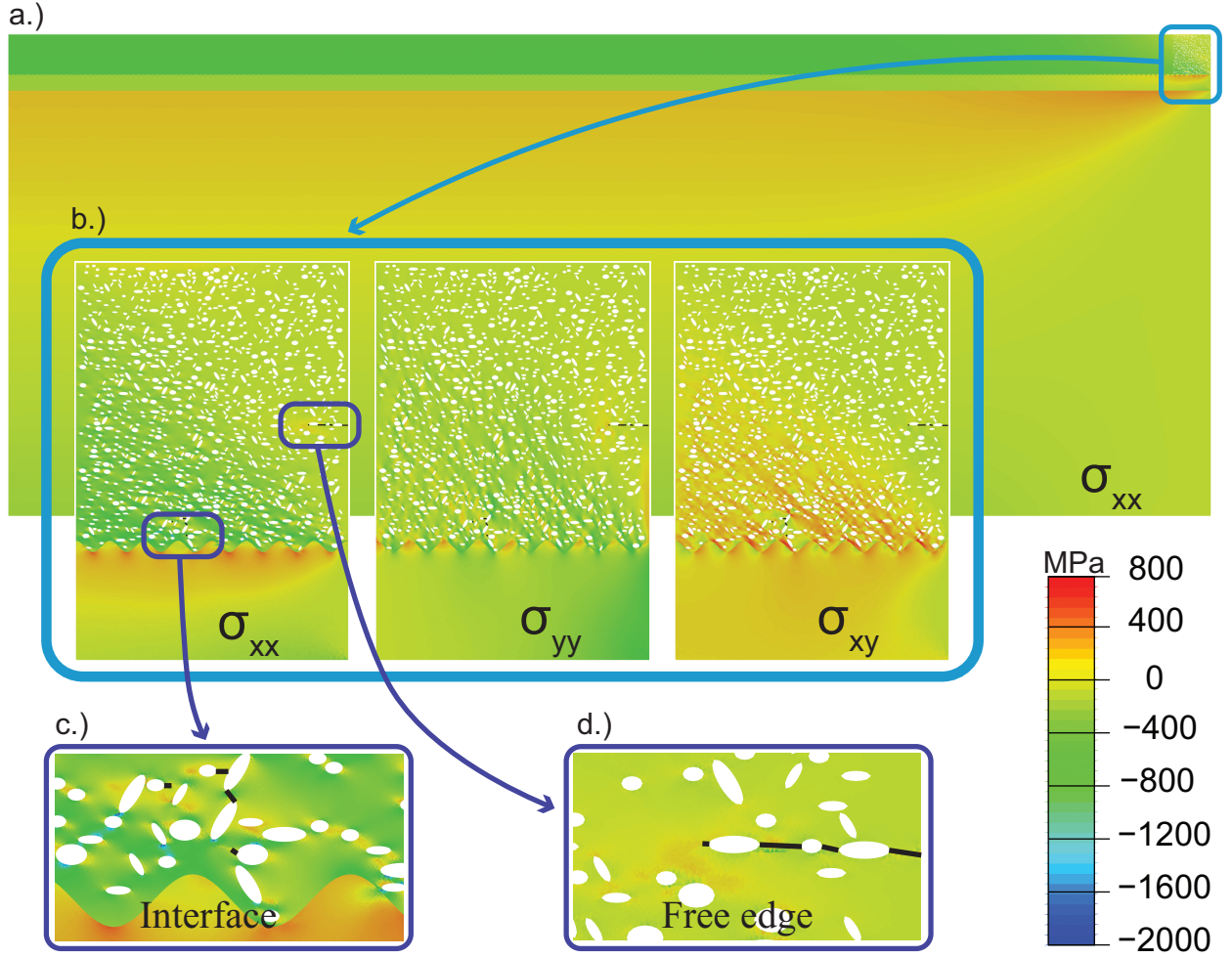
Figure 8: Stress distribution in TBC with realistically represented microstructural pores at T =30°C. a.) Stress variations (σ_{xx}) in the concurrent multiscale TBC model b.) Stress distribution in the TBC computational cell with explicitly modelled pores. c.) Mixed mode Cracking of interior TC layer close to BC due to pores and thermal mismatch stress. d.) Mode I cracking at the edge of the TC layer due to free edge effect.

3.3. Effect of TC fracture properties

The relative fracture properties of the TC layer with respect to the other layers of the TBC system influences the fracture behavior in terms of the location and pattern of crack evolution. The effect of this parameter is studied by considering two distinct parametric sets where the fracture ratio (f) is varied. The fracture ratio (f) is defined as

$$\begin{aligned} \sigma^{TC} &= f\sigma_0^{TC}, \\ G^{TC} &= fG_0^{TC} \end{aligned} \tag{1}$$

where f is the fracture ratio and σ_0^{TC} and G_0^{TC} are the fracture properties of the benchmark material. Note that both properties are varied using the same fracture ratio f and special
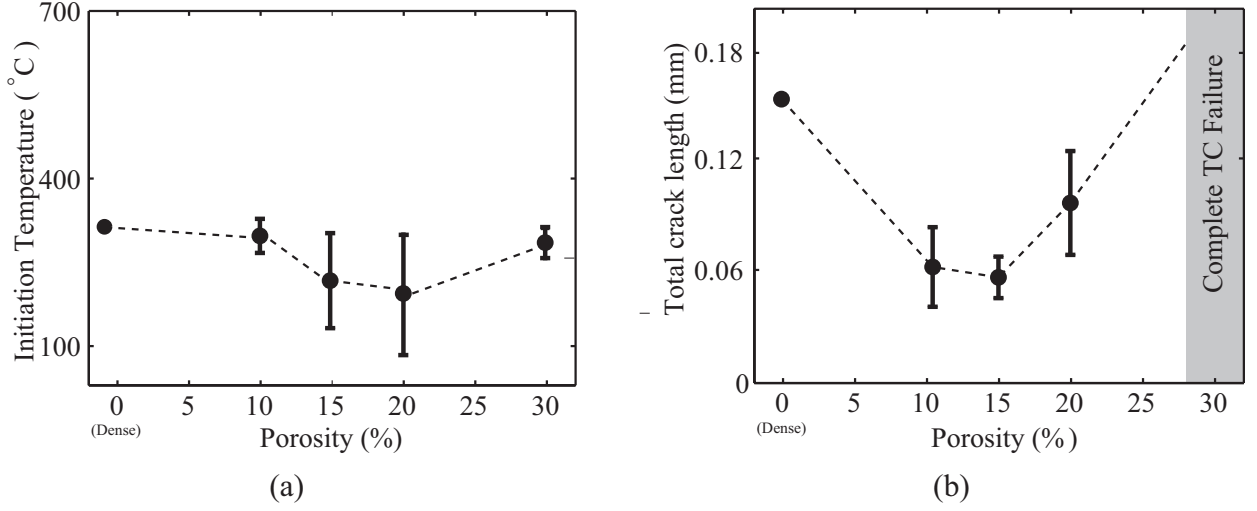
Figure 9: Variation of crack length with respect to loading temperature for five different realizations of TBC with the the same set of randomly represented microstructural pores.

attention is given to weaker materials ($f < 1$) as stronger material show limited damage.

In the first set, the normal fracture ratio (f_n) of the TC layer is varied with values of 0.625, 0.75, 0.875 and 1 while the shear fracture ratio (f_s) of the TC layer is fixed at 0.8. In the second set, the shear fracture ratio (f_s) is varied with values given by 0.625, 0.75, 0.875 and 1 for the normal fracture ratio (f_n) of 0.8. The range of TC fracture properties considered is based on the limits of TC strength values used for porous and dense TC layer [38].

The results of the study are summarized in terms of crack initiation temperature and total crack length in Fig. 10. The results corresponding to the normal fracture ratio variation are shown in Fig. 10.a and Fig. 10.b, and those corresponding to the variation of shear fracture are shown in Fig. 10.c. and Fig. 10.d. In general, it can be observed that the increase in normal fracture ratio delays the crack initiation in the TC layer as shown in Fig. Fig. 10.a. In case of shear fracture ratio, the effect on crack initiation is nil (refer Fig. 10.c.). This is because the normal strength, being always less than the shear strength for the TC layer, dominates the crack initiation behavior. In terms of crack length, the results shown in Fig. 10.b and Fig. 10.d are sensitive to the strength ratio provided the ratio is smaller than 0.9. For instance, complete failure of the TBC occurs when the fracture ratio is decreased below a value of 0.75 for both the cases. In terms of the crack pattern, it is observed that with a decrease in the strength, micro-cracks appear early in the TC layer. Upon the thermal loading process, the emanated micro-cracks near the TGO/TC interface tend to coalesce in the presence of stress concentrations due to the interface. Such a coalescence ultimately leads to the formation of a larger horizontal macro-crack, resulting in complete failure of the TBC. The critical fracture properties for the complete TBC failure is governed by the value of the fracture ratio with which the coalescence is favored.
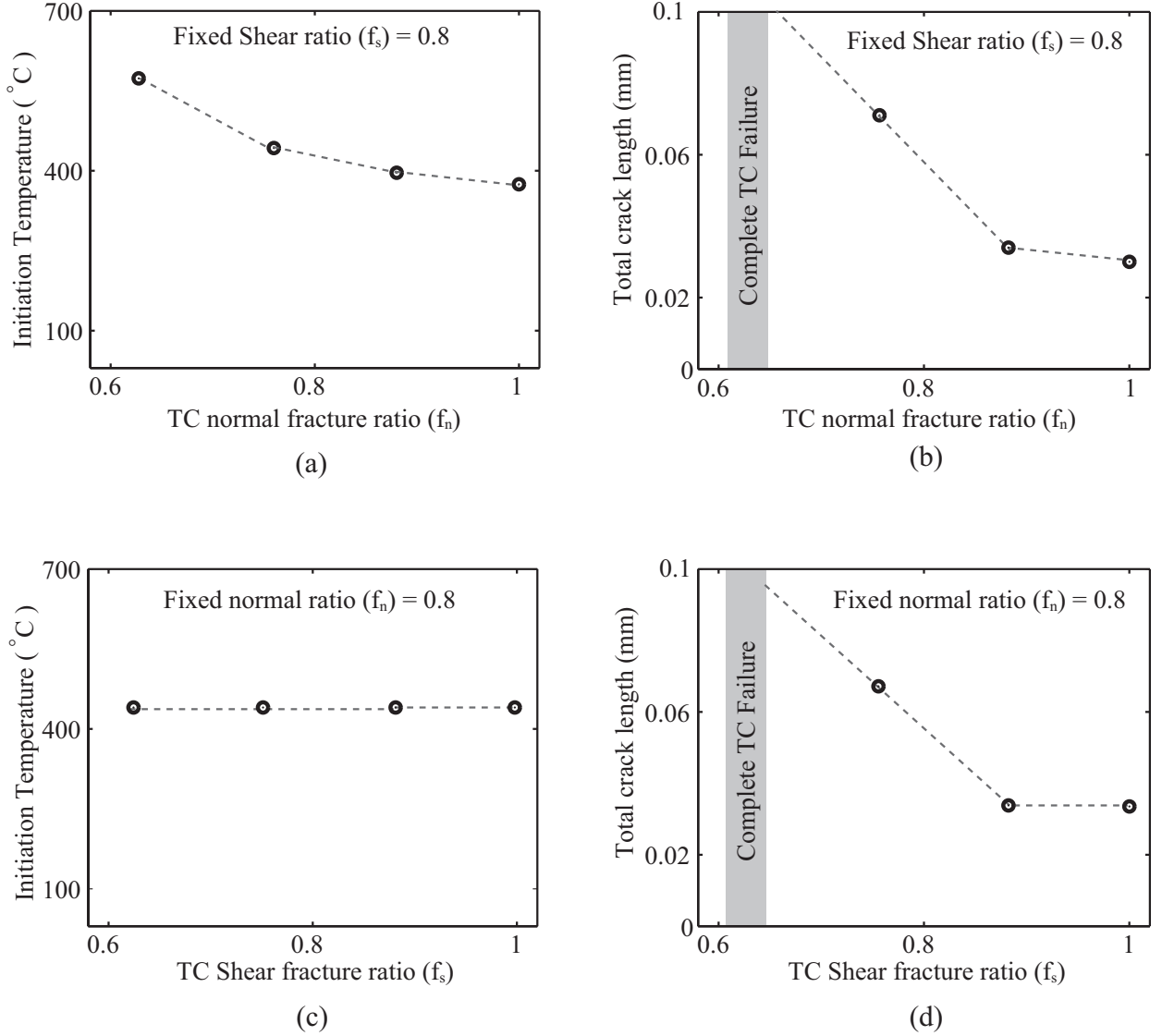
14

Figure 10: Variation of total crack length of TBC with random microstructural pores for different (a) Normal strength and (b) Shear strength values.

3.4. Effect of TGO thickness

In the simulations reported above, the thickness of the TGO layer is considered to be zero which corresponds to the initial thermal cycle of a TBC system. However, during cyclic operation, the TGO layer grows to a value in the range of 8 to 12 μm before onset of delamination failure [52, 51]. The presence of the TGO introduces additional thermal stresses due to its strong CTE mismatch with the underlying BC and TC layers, which in turn affects the crack evolution. Thus, in this section, the effect of TGO thickness on the TBC fracture behavior is investigated by considering different thickness values of the TGO, given by t_{TGO}= 0, 3, 6 and 9 μm. The simulations are carried out for the random pore features given in Table 3. Due to computational limitations, the TGO thickness values are
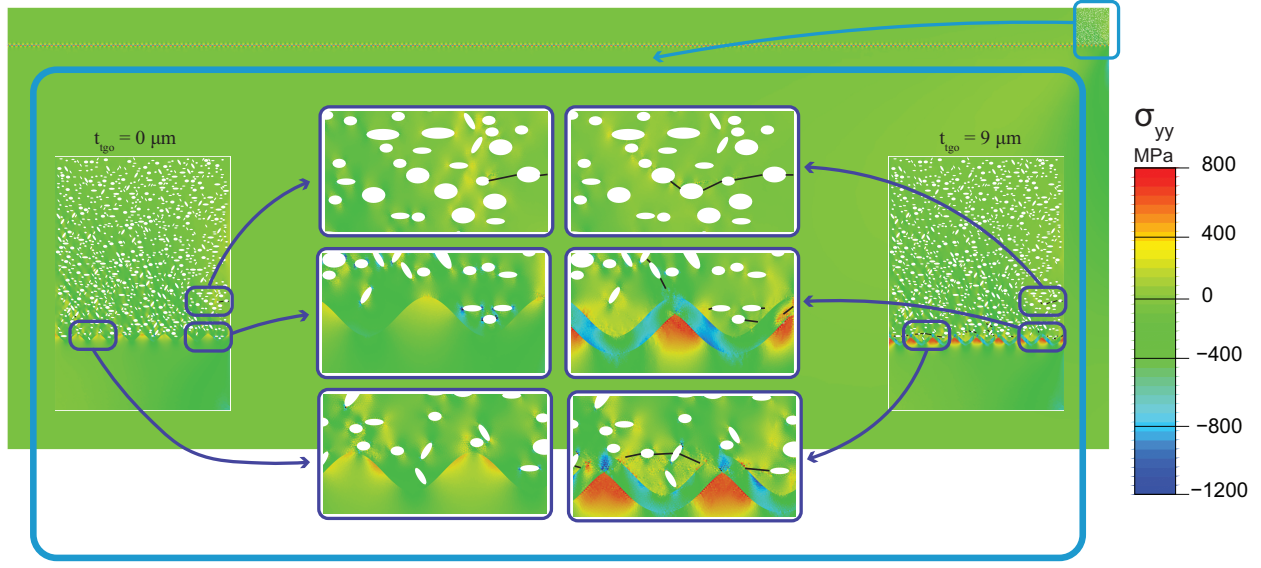
15

Figure 11: Stress distribution in TBC with random microstructural pores at T =30°C for TGO thickness of 0 μm and 9 μm

increased based on the assumption that no cracking did occur till the thickness of the TGO increased to the specified value.
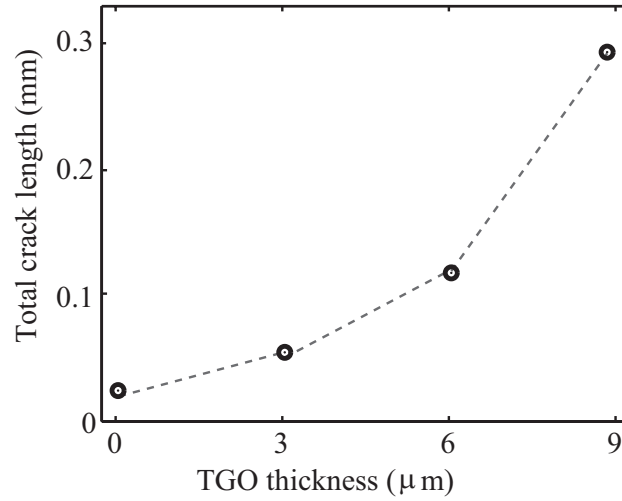

Figure 12: Variation of total crack length for different TGO thickness 0, 3, 6 and 9 μm with 15% random microstructural pores.

The effect of TGO thickness on the stress field and cracking behavior of the TBC is shown in Fig. 11 in terms of the normal stress distribution (σ_{yy}) corresponding to the TGO thickness of t_{TGO}= 0 μm (left inset) and 9 μm (right inset). Upon examining the stress distributions in the TBC without TGO (left inset in the figure), it can be seen that two different stress concentrations occur in the TBC, one arising due to the pores as discussed

16

before and the other due to the presence of dissimilar layers (TC and BC). Introduction of the TGO layer amplifies the stress concentration significantly around the interface as seen in Fig. 11 (right inset) which is attributed to the severe CTE mismatch between the TGO and the other two layers. This, in turn, alters the crack pattern as compared to the TBC system with no TGO layer. By comparing the results with and without the TGO, several distinctive observations can be made. The first key difference is that a higher TGO thickness leads to cracking in the TGO in addition to the cracking in the TC layer. This is not only because of the additional stress concentration effects as discussed above, but also due to the altered stress distribution in the proximity of the pores near the TGO layer. Upon closer observation, it can be seen that the stress fields near the pores are largely tensile in the presence of TGO as opposed to the compressive stress state of the pores in the case with zero TGO thickness. It is interesting to note that not only the presence of TGO layer leads to micro-cracks in and around it, but also it aggravates/accelerates the crack growth in the TC region which is relatively far away from the TGO layer. However, it is also worth mentioning that the stress distributions in the TC layer sufficiently far away from the TGO layer will be largely unaffected by the presence of TGO. In situations where there are edge cracks in the TC regions far from the TGO, it can be anticipated that the crack evolution will be least affected by the presence of the TGO layer.

The results of the simulations conducted for different values of the TGO thickness are summarized in the Fig. 12. The total crack length is plotted as a function of the TGO thickness. From the results, it can be observed that increasing the TGO thickness decreases the integrity of the TBC system [52]. Indeed the total crack length at the end of the thermal loading step increases approximately quadratically as a function of TGO thickness.

4. Conclusions

The effect of microstructural porosity on the fracture behavior of the TBC is analyzed using cohesive elements-based finite element method. Geometric and material parameters such as TGO thickness, pore characteristics (such as aspect ratio, size, volume fraction and orientation), and TC fracture properties are studied through parametric analyses. Two simulation sets are considered: one with a controlled pore characteristics and one with random pore characteristics. For the controlled microstructure, the results of the parametric studies are reported in terms of the crack initiation temperature and total crack length, whereby several pore features were found to exhibit a significant influence on the failure behavior. The following conclusions are drawn from the parametric finite element investigations.

1. Porosity plays a significant role in improving the fracture resistance of the TBC. However, porosity above a critical value leads to early failure of the TBC.
2. Increasing the pore size decreases the TBC integrity where the crack initiation temperature and the crack length increase with increase in pore size. Both the crack initiation temperature and the total crack length showed a linear variation with respect to pore size
3. Pore aspect ratio exhibited a similar influence as that of the pore size, where the initiation temperature and the crack length increases with pore aspect ratio

17

4. The crack initiation temperature decreases with increase in pore orientation angle. In terms of the crack length, complete failure occurs for pore orientations that lie between 45 and 90 deg.

For the microstructure with random pore characteristics, the simulations indicate the following:

1. The porosity is the main parameter that predicts the total crack length compared to other pore characteristics. Nonetheless, the random distribution of pore size, pore area and pore orientation results in a large scatter in data.
2. On the effect of the material parameter, namely the TC fracture properties, the crack initiation temperature is slightly influenced. However, in terms of crack length, complete TBC failure is observed when both the normal and shear fracture are reduced to a value below a critical level.
3. The TGO thickness showed a significant effect on the failure behavior. The crack initiation temperature linearly increases with increasing TGO thickness, whereas the crack length increased quadratically.

The results and the insights could serve for understanding the effect of pore defects on failure behavior, which in turn can aid in engineering or designing the microstructure for improved performance/lifetime. To summarize the major findings to help in optimizing the TBC behavior, a porous TBC system with smaller pore size, circular pores (or if the pores are elliptical, it should have small aspect ratio), close to zero degree orientation and higher TC fracture properties would result in an optimal TBC system with enhanced thermal cycling integrity.

References

[1] T. Hille, A. Suiker, S. Turteltaub, Microcrack nucleation in thermal barrier coating systems, Engineering Fracture Mechanics 76 (6) (2009) 813–825 (2009).
[2] A. G. Evans, D. Mumm, J. Hutchinson, G. Meier, F. Pettit, Mechanisms controlling the durability of thermal barrier coatings, Progress in materials science 46 (5) (2001) 505–553 (2001).
[3] Y. Song, W. Wu, M. Qin, D. Li, Y. Liu, S. Ai, T. Wang, Effect of geometric parameter on thermal stress generation in fabrication process of double-ceramic-layers thermal barrier coating system, Journal of the European Ceramic Society 38 (11) (2018) 3962–3973 (2018).
[4] C. Li, X. Zhang, Y. Chen, J. Carr, S. Jacques, J. Behnsen, M. di Michiel, P. Xiao, R. Cernik, Understanding the residual stress distribution through the thickness of atmosphere plasma sprayed (APS) thermal barrier coatings (TBCs) by high energy synchrotron XRD; digital image correlation (DIC) and image based modelling, Acta Materialia 132 (2017) 1–12 (jun 2017).
[5] K. W. Schlichting, N. P. Padture, E. H. Jordan, M. Gell, Failure modes in plasma-sprayed thermal barrier coatings, Materials Science and Engineering A 342 (1-2) (2003) 120–130 (feb 2003).

[6] Z. Zhang, J. Kameda, A. H. Swanson, S. Sakurai, M. Sato, Effects of porosity and thermal ageing on in-plane cracking behavior of thermal barrier coatings, in: W. J. Meng, A. Kumar, G. L. Doll, Y. T. Cheng, S. Veprek, Y. W. Chung (Eds.), Surface Engineering 2001 - Fundamentals and Applications, Vol. 697, Materials Research Society, Warrendale, 2001, pp. 95–100 (2001).

[7] W. Nowak, D. Naumenko, G. Mor, F. Mor, D. E. Mack, R. Vassen, L. Singheiser, W. J. Quadakkers, Effect of processing parameters on MCrAlY bondcoat roughness and lifetime of APS-TBC systems, Surface and Coatings Technology 260 (2014) 82–89 (dec 2014).

[8] A. N. Khan, J. Lu, Manipulation of air plasma spraying parameters for the production of ceramic coatings, Journal of Materials Processing Technology 209 (5) (2009) 2508–2514 (mar 2009).

[9] H. Guo, R. Vaßen, D. Stöver, Atmospheric plasma sprayed thick thermal barrier coatings with high segmentation crack density, Surface and Coatings Technology 186 (3) (2004) 353–363 (sep 2004).

[10] A. Kulkarni, A. Vaidya, A. Goland, S. Sampath, H. Herman, Processing effects on porosity-property correlations in plasma sprayed yttria-stabilized zirconia coatings, Materials Science and Engineering A 359 (1-2) (2003) 100–111 (oct 2003).

[11] D. Schwingel, R. Taylor, T. Haubold, J. Wigren, C. Gualco, Mechanical and thermophysical properties of thick PYSZ thermal barrier coatings: correlation with microstructure and spraying parameters, Surface and Coatings Technology 108-109 (1998) 99–106 (oct 1998).

[12] U. Klement, J. Ekberg, S. Creci, S. T. Kelly, Porosity measurements in suspension plasma sprayed YSZ coatings using NMR cryoporometry and X-ray microscopy, Journal of Coatings Technology and Research 15 (4) (2018) 753–757 (jul 2018).

[13] D. F. Zambrano, A. Barrios, L. E. Tobón, C. Serna, P. Gómez, J. D. Osorio, A. Toro, Thermal properties and phase stability of Yttria-Stabilized Zirconia (YSZ) coating deposited by Air Plasma Spray onto a Ni-base superalloy, Ceramics International 44 (4) (2018) 3625–3635 (mar 2018).

[14] X. Qiao, Y. M. Wang, W. X. Weng, B. L. Liu, Q. Li, Influence of pores on mechanical properties of plasma sprayed coatings: Case study of YSZ thermal barrier coatings, Ceramics International 44 (17) (2018) 21564–21577 (dec 2018).

[15] F. Cernuschi, I. O. Golosnoy, P. Bison, A. Moscatelli, R. Vassen, H. P. Bossmann, S. Capelli, Microstructural characterization of porous thermal barrier coatings by IR gas porosimetry and sintering forecasts, Acta Materialia 61 (1) (2013) 248–262 (jan 2013).

[16] J. Zhang, V. Desai, Evaluation of thickness, porosity and pore shape of plasma sprayed TBC by electrochemical impedance spectroscopy, Surface and Coatings Technology 190 (1) (2005) 98–109 (jan 2005).

[17] P. Strunz, G. Schumacher, R. Vassen, A. Wiedenmann, In situ SANS study of pore microstructure in YSZ thermal barrier coatings, Acta Materialia 52 (11) (2004) 3305–3312 (jun 2004).

[18] A. J. Allen, J. Ilavsky, G. G. Long, J. S. Wallace, C. C. Berndt, H. Herman, Microstructural characterization of yttria-stabilized zirconia plasma-sprayed deposits using multiple small-angle neutron scattering, Acta Materialia 49 (9) (2001) 1661–1675 (may 2001).

[19] G. Boissonnet, G. Bonnet, A. Pasquet, N. Bourhila, F. Pedraza, Evolution of thermal insulation of plasma-sprayed thermal barrier coating systems with exposure to high temperature, Journal of the European Ceramic Society (2019).

[20] Y. Xiao, E. Ren, M. Hu, K. Liu, Y. Xiao, E. Ren, M. Hu, K. Liu, Effect of Particle In-Flight Behavior on the Microstructure and Fracture Toughness of YSZ TBCs Prepared by Plasma Spraying, Coatings 8 (9) (2018) 309 (sep 2018).

[21] A. Kulkarni, Z. Wang, T. Nakamura, S. Sampath, A. Goland, H. Herman, J. Allen, J. Ilavsky, G. Long, J. Frahm, R. W. Steinbrech, Comprehensive microstructural characterization and predictive property modeling of plasma-sprayed zirconia coatings, Acta Materialia 51 (9) (2003) 2457–2475 (may 2003).

[22] L. Wang, Y. Wang, X. G. Sun, J. Q. He, Z. Y. Pan, Y. Zhou, P. L. Wu, Influence of pores on the thermal insulation behavior of thermal barrier coatings prepared by atmospheric plasma spray, Materials and Design 32 (1) (2011) 36–47 (jan 2011).

[23] K. W. Schlichting, N. P. Padture, P. G. Klemens, Thermal conductivity of dense and porous yttria-stabilized zirconia, Journal of Materials Science 36 (12) (2001) 3003–3010 (2001).

[24] I. Sevostianov, M. Kachanov, Plasma-sprayed ceramic coatings: Anisotropic elastic and conductive properties in relation to the microstructure; Cross-property correlations, Materials Science and Engineering A 297 (1-2) (2001) 235–243 (jan 2001).

[25] T. Nakamura, G. Qian, C. C. Berndt, Effects of pores on mechanical properties of plasma-sprayed ceramic coatings, Journal of the American Ceramic Society 83 (3) (2000) 578–584 (dec 2000).

[26] F. Cernuschi, S. Ahmaniemi, P. Vuoristo, T. Mäntylä, Modelling of thermal conductivity of porous materials: Application to thick thermal barrier coatings, Journal of the European Ceramic Society 24 (9) (2004) 2657–2667 (aug 2004).

[27] S. Gu, T. J. Lu, D. D. Hass, H. N. Wadley, Thermal conductivity of zirconia coatings with zig-zag pore microstructures, Acta Materialia 49 (13) (2001) 2539–2547 (aug 2001).

[28] M. Gupta, P. Nylén, J. Wigren, A modelling approach to designing microstructures in thermal barrier coatings, Journal of Ceramic Science and Technology 4 (2) (2013) 85–92 (2013).

[29] Z. Wang, A. Kulkarni, S. Deshpande, T. Nakamura, H. Herman, Effects of pores and interfaces on effective properties of plasma sprayed zirconia coatings, Acta Materialia 51 (18) (2003) 5319–5334 (oct 2003).

[30] M. Yang, Y. Zhu, X. Wang, S. Guo, J. Hu, L. Zhao, Y. Chu, Effect of five kinds of pores shape on thermal stress properties of thermal barrier coatings by finite element method, Ceramics International 43 (13) (2017) 9664–9678 (sep 2017).

[31] M. Ranjbar-far, J. Absi, G. Mariaux, D. Smith, Crack propagation modeling on the interfaces of thermal barrier coating system with different thickness of the oxide layer and different interface morphologies, Materials & Design 32 (10) (2011) 4961–4969 (dec 2011).

[32] T. Hille, S. Turteltaub, A. Suiker, Oxide growth and damage evolution in thermal barrier coatings, Engineering Fracture Mechanics 78 (10) (2011) 2139–2152 (jul 2011).

[33] M. Białas, Finite element analysis of stress distribution in thermal barrier coatings, Surface and Coatings Technology 202 (24) (2008) 6002–6010 (aug 2008).

[34] L. Wang, D. C. Li, J. S. Yang, F. Shao, X. H. Zhong, H. Y. Zhao, K. Yang, S. Y. Tao, Y. Wang, Modeling of thermal properties and failure of thermal barrier coatings with the use of finite element methods: A review, Journal of the European Ceramic Society 36 (6) (2016) 1313–1331 (May 2016).

[35] S. Ozaki, Y. Aoki, T. Osada, K. Takeo, W. Nakao, Finite element analysis of fracture statistics of ceramics: Effects of grain size and pore size distributions, Journal of the American Ceramic Society 101 (7) (2018) 3191–3204 (2018).

[36] L. Wang, Q. Fan, Y. Liu, G. Li, H. Zhang, Q. Wang, F. Wang, Simulation of damage and failure processes of thermal barrier coatings subjected to a uniaxial tensile load, Materials and Design 86 (2015) 89–97 (dec 2015).

[37] W. G. Sloof, Self-Healing Thermal Barrier Coatings for Prolonged Lifetime (funded by EU-FP7). URL http://www.sambaproject.eu/

[38] J. Krishnasamy, S. A. Ponnusami, S. Turteltaub, S. van der Zwaag, Modelling the fracture behaviour of thermal barrier coatings containing healing particles, Materials & Design 157 (2018) 75–86 (nov 2018).

[39] M. Martena, D. Botto, P. Fino, S. Sabbadini, M. Gola, C. Badini, Modelling of TBC system failure: Stress distribution as a function of TGO thickness and thermal expansion mismatch, Engineering Failure Analysis 13 (3) (2006) 409–426 (apr 2006).

[40] K. P. Jonnalagadda, R. Eriksson, K. Yuan, X.-H. Li, X. Ji, Y. Yu, R. L. Peng, A study of damage evolution in high purity nano tbcs during thermal cycling: A fracture mechanics based modelling approach, Journal of the European Ceramic Society 37 (8) (2017) 2889–2899 (2017).

[41] J. W. Hutchinson, A. G. Evans, On the delamination of thermal barrier coatings in a thermal gradient, Surface and Coatings Technology 149 (2-3) (2002) 179–184 (jan 2002).

[42] R. Vaßen, G. Kerkhoff, D. Stöver, Development of a micromechanical life prediction model for plasma sprayed thermal barrier coatings, Materials Science and Engineering A 303 (1-2) (2001) 100–109 (may 2001).

[43] A. Hillerborg, M. Modéer, P.-E. Petersson, Analysis of crack formation and crack growth in concrete by means of fracture mechanics and finite elements, Cement and Concrete Research 6 (6) (1976) 773–781

(nov 1976).

[44] C. Geuzaine, J.-F. Remacle, Gmsh: a three-dimensional finite element mesh generator with built-in pre-and post-processing facilities, International Journal for Numerical Methods in Engineering 79 (11) (2009) 1–24 (2009).

[45] S. Choi, N. Bansal, Mechanical behavior of zirconia/alumina composites, Ceramics International 31 (1) (2005) 39–46 (jan 2005).

[46] H. Zhao, Z. Yu, H. N. Wadley, The influence of coating compliance on the delamination of thermal barrier coatings, Surface and Coatings Technology 204 (15) (2010) 2432–2441 (2010).

[47] M. Karger, R. Vaßen, D. Stöver, Atmospheric plasma sprayed thermal barrier coatings with high segmentation crack densities: Spraying process, microstructure and thermal cycling behavior, Surface and Coatings Technology 206 (1) (2011) 16–23 (oct 2011).

[48] D. M. Liu, Influence of porosity and pore size on the compressive strength of porous hydroxyapatite ceramic, Ceramics International 23 (2) (1997) 135–139 (jan 1997).

[49] I. Sabree, J. E. Gough, B. Derby, Mechanical properties of porous ceramic scaffolds: Influence of internal dimensions, Ceramics International 41 (7) (2015) 8425–8432 (aug 2015).

[50] X. Li, S. Jiang, Y. Ye, S. Liu, Z. Xu, Y. Tan, D. Yang, Influence of random pore defects on failure mode and mechanical properties of SiC ceramics under uniaxial compression using discrete element method, Ceramics International 44 (18) (2018) 22271–22282 (dec 2018).

[51] O. Trunova, T. Beck, R. Herzog, R. Steinbrech, L. Singheiser, Damage mechanisms and lifetime behavior of plasma sprayed thermal barrier coating systems for gas turbines—Part I: Experiments, Surface and Coatings Technology 202 (20) (2008) 5027–5032 (jul 2008).

[52] H. Dong, G.-J. Yang, C.-X. Li, X.-T. Luo, C.-J. Li, Effect of TGO Thickness on Thermal Cyclic Lifetime and Failure Mode of Plasma-Sprayed TBCs, Journal of the American Ceramic Society 97 (4) (2014) 1226–1232 (apr 2014).